Electrical conductivity of iron in Earth's core from microscopic Ohm's law

Kushal Ramakrishna, Mani Lokamani, Andrew Baczewski, Jan Vorberger, and Attila Cangi

Phys. Rev. B **107**, 115131 — Published 14 March 2023

DOI: 10.1103/PhysRevB.107.115131

Electrical Conductivity of Iron in Earth's Core from Microscopic Ohm's Law

Kushal Ramakrishna,[1,*] Mani Lokamani,[2] Andrew Baczewski,[3] Jan Vorberger,[4] and Attila Cangi[1,†]

[1] *Center for Advanced Systems Understanding (CASUS), Helmholtz-Zentrum Dresden-Rossendorf (HZDR), 02826 Görlitz, Germany*
[2] *Information Services and Computing, Helmholtz-Zentrum Dresden-Rossendorf (HZDR), 01328 Dresden, Germany*
[3] *Center for Computing Research, Sandia National Laboratories, Albuquerque NM 87185 USA*
[4] *Insitute of Radiation Physics, Helmholtz-Zentrum Dresden-Rossendorf (HZDR), 01328 Dresden, Germany*

(Dated: March 3, 2023)

Understanding the electronic transport properties of iron under high temperatures and pressures is essential for constraining geophysical processes. The difficulty of reliably measuring these properties under conditions prevalent in Earth's core calls for first-principles methods that can support diagnostics. We present results on the electrical conductivity obtained by simulating the microscopic Ohm's law using time-dependent density functional theory and place them in the context of recent experimental measurements.

I. INTRODUCTION

Iron is the most abundant element by mass on planet Earth [1]. It makes up the majority of its liquid outer core and solid inner core [2, 3], which is exposed to temperatures of about 6000 K and pressures of about 300 GPa. Understanding the properties of iron under these extreme conditions is of great geophysical importance because they determine the internal structure of Earth. Likewise, the behavior of iron under elevated temperatures and pressures also plays a major role in materials science. A wide range of novel steel micro-structures can be produced with minor changes in composition and proper thermal treatment of iron-based alloys [4, 5].

The iron phase diagram [6–11] and its equation of state [7, 8, 12–19] have been well studied in the past decades. Beyond equation-of-state data, the transport properties of iron, such as its electrical and thermal conductivity, are intricately related to the geophysical dynamics that take place in the planetary interior. Most prominently, the heat flux between the planetary core and mantle drives the dynamo action [20, 21] which generates the magnetic field of the Earth.

However, information on electronic transport properties under the conditions of Earth's core is sparse. This is due to the difficulties of achieving accurate measurements in experiments. These are commonly performed in diamond-anvil cells (DAC) [22–24], with wire-heating techniques [25, 26], as well as using static and dynamic shock-compression [27–29]. Shock compression techniques combined with x-ray Thomson scattering (XRTS) provide diagnostics for the dynamical and static conductivity, which have been measured in warm dense metals [30]. Most recently, terahertz transmission measurements of the time-resolved electrical conductivity in warm dense gold [31] have shown promise as a viable approach for further probing transport properties under extreme conditions.

The above-mentioned experiments with laser-heated diamond anvil cells [23, 24] have led to a notable controversy in the measurement of electronic transport properties in iron at the core-mantle boundary (CMB) and Earth-core conditions [32]. Ohta *et al.* [23] infer a thermal conductivity of 226 $\mathrm{Wm^{-1}K^{-1}}$ by measuring the electrical resistance of iron wires and converting it into a thermal conductivity using the Wiedemann-Franz law. On the other hand, Konôpková *et al.* [24] measured the thermal diffusion rate for heat transferred between the ends of solid iron samples, inferring a thermal conductivity of 30 $\mathrm{Wm^{-1}K^{-1}}$ from the agreement with a finite-element model. The discrepancy in these measurements has deep implications for predicting the age of the Earth [32]. Since the uncertainty in the electrical conductivity, both from experiment and theory, is so high, reliable knowledge about the fundamental processes generating Earth's magnetic field is lacking as well. Due to the disagreement among existing experimental data, computational modeling of electronic transport properties under extreme conditions is indispensable in supporting current and future efforts in further probing these properties under conditions prevalent in Earth's core [33].

The pioneering theoretical works use the Kubo-Greenwood (KG) formula [34] and have been applied in modeling degenerate plasma states [35–37] and liquid metals [38–40]. These evaluate the KG formula using the Kohn-Sham (KS) orbitals, eigenvalues, and occupation numbers obtained from density functional theory (DFT) calculations at finite electronic temperature [41–43]. Most recently, Korell *et al.* [44] have investigated the effects of spin-polarization on the electrical conductivity obtained from the KG formula, specifically for the paramagnetic state of liquid iron. This formulation has also been used for evaluating the electrical and thermal conductivity of iron and iron-silicon mixtures at Earth-core conditions [45–47]. The direct use of KS quanti-

* k.ramakrishna@hzdr.de
† a.cangi@hzdr.de

ties in the KG formula, however, is based on a response function lacking an interaction kernel that is needed to capture collective effects. This is especially relevant under the conditions when the electrons in iron are strongly correlated [48].

Improvements in transport properties of iron at extreme conditions computed using DFT are possible by means of dynamical mean field theory (DMFT) [49]. This approach takes into account the on-site Coulomb interaction, which is particularly strong for the localized *3d* electrons in iron [50]. The net conductivity consists of electron-lattice scattering usually evaluated with the KG formula and the electron-electron scattering (EES) evaluated with DMFT which takes into account the electronic correlations and the thermal disorder. EES contributions in HCP iron are reported to be insignificant compared to electron-lattice scattering at the conditions of Earth's core but have important contributions to the total thermal conductivity [51].

A viable alternative to the KG formula is linear response time-dependent density functional theory (LR-TDDFT) [52]. While KS orbitals are used to calculate a non-interacting response function, the Hartree and exchange-correlation (XC) kernels are used to obtain an interacting response function that includes electron-electron correlations. Furthermore, LR-TDDFT yields full wavenumber and frequency-resolved transport properties. This method has recently been assessed in detail for solid and liquid aluminum [53, 54]. However, the calculations using LR-TDDFT [55] rely on matrix diagonalization, which might become restrictive for large systems or high temperatures.

In this work, we compute the electrical conductivity directly from the microscopic formulation of Ohm's law. This is achieved using the real-time formalism of TDDFT (RT-TDDFT) [56–58]. By applying a weak external field, the electronic response, which determines optical properties and electronic transport properties, is extracted [59–62]. For certain regimes of electronic excitation and large systems, RT-TDDFT can be computationally more efficient than LR-TDDFT. As in LR-TDDFT, the response function computed using RT-TDDFT captures collective effects that are not captured in the standard approach using the KG formula.

II. METHODS

The microscopic formulation of Ohm's law describes how an external electric field $\boldsymbol{E}(\omega)$ gives rise to an induced electric current

$$\boldsymbol{J}(\omega) = \boldsymbol{\sigma}(\omega)\,\boldsymbol{E}(\omega)\,, \tag{1}$$

where the constant of proportionality can be identified as the electrical conductivity $\boldsymbol{\sigma}(\omega)$. Note that Ohm's law is formulated in the frequency domain and that both the current and the electric field are vectors, while the conductivity is a tensor. Also note that we adopt Hartree atomic units, i.e., $\hbar = e = m_e = a_0 = 1$, so energies are expressed in Hartrees and lengths in Bohr radii.

We compute the induced current on the atomistic level by using RT-TDDFT. By applying an electric field $\boldsymbol{E}(t) = -(1/c)(\partial\boldsymbol{A}/\partial t)$, where $\boldsymbol{A}$ is the impressed vector potential and c is the speed of light, we obtain the induced time-dependent current density $\boldsymbol{j}(\boldsymbol{r},t) = \Im[\sum_i^N \phi^*_{n,k}(\boldsymbol{r},t)\nabla\phi_{n,k}(\boldsymbol{r},t)] + n(\boldsymbol{r},t)\boldsymbol{A}_S(\boldsymbol{r},t)/c$. When integrated over the spatial coordinates, it yields a time-dependent electric current $\boldsymbol{J}(t)$. By taking the Fourier transform, we obtain Ohm's law in the frequency domain as denoted in Eq. (1). The time-dependent current density is obtained by solving the time-dependent KS equations

$$\hat{H}_S\phi_{n,k}(\boldsymbol{r},t) = i\frac{\partial}{\partial t}\phi_{n,k}(\boldsymbol{r},t) \tag{2}$$

for the KS orbitals $\phi_{n,k}(\boldsymbol{r},t)$. The effective Hamiltonian is

$$\hat{H}_S = \frac{1}{2}\left[-i\nabla + \frac{1}{c}\boldsymbol{A}_S(\boldsymbol{r},t)\right]^2 + V_S(\boldsymbol{r},t) \tag{3}$$

where $V_S(\boldsymbol{r},t) = V_{ext}(\boldsymbol{r},t) + V_H(\boldsymbol{r},t) + V_{XC}(\boldsymbol{r},t)$ is the KS potential which is a sum of the external, the Hartree, and XC potentials, while the effective vector potential $\boldsymbol{A}_S(\boldsymbol{r},t) = \boldsymbol{A}(\boldsymbol{r},t) + \boldsymbol{A}_{XC}(\boldsymbol{r},t)$ comprises the sum of the external vector potential and the XC contribution. The following RT-TDDFT results are obtained from an all-electron full-potential linearized augmented plane wave (FP-LAPW) method [65] as implemented in the Elk [66] and Exciting [67, 68] codes. For the sake of clarity and reproducibility, we provide a comprehensive description of all computational details and simulation parameters in the Supplemental Material [69].

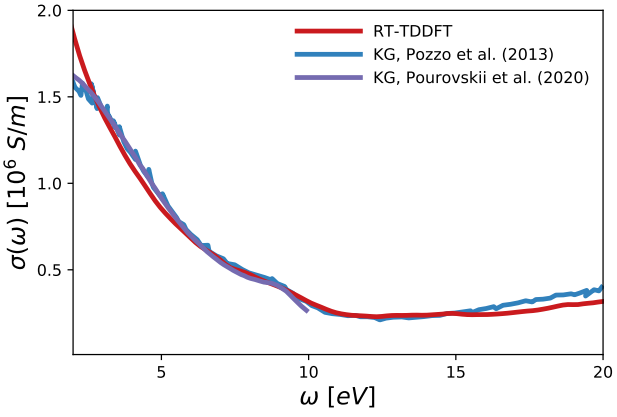

FIG. 1. Dynamical electrical conductivity under Earth-core conditions ($T = 6350$ K, $P = 322$ GPa) from Ohm's law based on our RT-TDDFT calculations (red). This is compared with previous works using the KG formula based on static DFT calculations at a slightly higher pressure of 328 GPa [63] (blue) and at a lower temperature of $T = 5802$ K and slightly lower pressure of $P = 310$ GPa [64] (violet).

We begin with computing the frequency-dependent response of the electrons in iron at a pressure of 322 GPa and a temperature of 6350 K as found in Earth's core. To that end, we first prepare an appropriate initial electronic state. We follow the common procedure of generating uncorrelated atomic snapshots from Born-Oppenheimer molecular dynamics simulations based on static DFT at the given temperature and pressure. Here, our simulation cells contain 16 iron atoms. Subsequently, we apply a step-like vector potential and solve Eq. (2) for a duration of up to t =1000 a.u. As commonly assumed in TDDFT, we invoke the adiabatic approximation which means that we neglect the temporal non-locality of the time-dependent KS potential and evaluate a ground-state XC functional on the density at time t. We follow this common procedure and employ the so-called adiabatic local density approximation [52]. Based on the solutions $\phi_{n,k}(\boldsymbol{r},t)$, we calculate the time-dependent current density $\boldsymbol{j}(\boldsymbol{r},t)$ which we integrate over the spatial coordinates to obtain the electric current $\boldsymbol{J}(t)$. The frequency-dependent, i.e., dynamical electrical conductivity is then extracted from the electric current based on Ohm's law as given in Eq. (1). Care has to be taken in the choice of parameters for the external vector potential and for the Fourier transform of the macroscopic current from the time to the frequency domain. These details along with the choice of computational and methodological parameters are also included in the Supplemental Material [69].

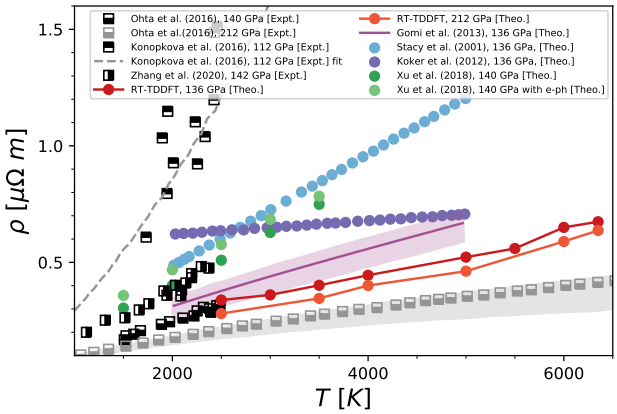

FIG. 2. Electrical resistivity and its temperature dependence at 136(±5) GPa and 212(±6) GPa. Results of diamond anvil cell measurements were reported by Ohta *et al.* [23] (lower filled black and grey squares), Zhang *et al.* [70] (right filled black squares) and by Konôpková *et al.* [24] (upper filled black squares). The electrical resistivity predicted by Ohm's law based on our RT-TDDFT calculations (red circles) are compared with first-principles calculations by Xu *et al.* [71] (green circles), interpolated results of Stacey *et al.* [72] (blue curve), a modified Bloch-Grüneisen model of Koker *et al.* [39] (violet curve), and a Bloch-Grüneisen model including resistivity saturation by Gomi *et al.* [22] (purple curve).

III. RESULTS

Fig. 1 illustrates the result of our RT-TDDFT calculations (red curve) with an energy resolution of 0.17 eV which is proportional to the inverse of the total propagation time. The calculations converge quickly given a sufficient set of KS orbitals, even for a modest size of the supercell. We compare our calculations with prior results obtained from using the KG formula based on static DFT [63, 64]. In this particular case, all methods yield similar results except for a discrepancy in the $\omega \to 0$ limit which corresponds to the DC conductivity. Note that the KG results are generally more susceptible to finite-size effects and are very sensitive to the location and density of the KS eigenvalues.

Next, we come to the central result presented in Fig. 2 where we compare the predictions of our RT-TDDFT calculations with the discordant experimental measurements reported by Ohta *et al.* [23], Zhang *et al.* [70] and Konôpková *et al.* [24]. In order to compare our calculations with the reported experiments, we use the DC conductivity.

Shown in Fig. 2 is the behavior of the electrical resistivity ρ (the inverse of the conductivity) as a function of the temperature at fixed, high pressures. The experimental DAC measurements reported by Ohta *et al.* [23] (lower filled black and grey squares) and Zhang *et al.* [70] (right filled black squares) are contrasted with those by Konôpková *et al.* [24] (upper filled black squares). Note that the data by Konôpková *et al.* are based on their thermal conductivity measurements which we have converted into an electrical resistivity using the Wiedemann-Franz law [73] with a Lorenz number 2.44×10^{-8} WΩK^{-2}. In addition, their fit (grey dashed) to the experimental data is also shown. The proportionality $\rho \propto T$ (quasi-linear) at these conditions is observed in other results too, particularly in the Bloch-Grüneisen model (purple curve) based on the Debye temperature [74] lying between the experimental results of Ohta *et al.* and Zhang *et al.*. The net effect of increasing pressure is to decrease the resistivity as is also reported in experiments [22, 70, 75] and other theoretical work [62] because the smaller amplitude of ionic vibrations is responsible for an increase in the mean free path of the electrons. The striking feature of this plot is that the electrical resistivity predicted by Ohm's law based on our RT-TDDFT calculations agrees well with the measurements of Ohta *et al.*, particularly with the data points at a pressure of 140 GPa and a temperature of 2500 K (red circles) which are considerably lower than the measurements by Zhang *et al.* This suggests our calculations would reasonably be in the range of both the measurements by Ohta and Zhang *et al.* at lower temperatures (<2000 K). Reasonable agreement between the two aforementioned measurements but at room temperature (300 K) is demonstrated in a recent theoretical effort by Ramakrishna *et al.* [62]. Other prior works including the interpolated results of Stacey *et*

al. [72] (blue curve), the Bloch-Grüneisen model of Koker *et al.* [39] (violet curve), and the first-principles calculations by Xu *et al.* [71] including the electron-phonon contribution (green circles) seem also to be in reasonable agreement with the results by Zhang *et al.*. Note that the contribution of EES in HCP iron to the resistivity under Earth-core conditions is well assessed by Pourovskii *et al.* [51] in terms of DMFT leading to a behavior $\rho_{EES} \propto T^2$. However, the effects of EES are negligible for the data points in the range of 2500−3000 K.

For a direct comparison with experiments, we convert our calculated resistivities shown in Fig. 2 into a thermal conductivity (electronic component) using the Wiedemann-Franz law. At the temperatures and pressures relevant to the CMB (P∼136 GPa, T∼4000 K), we hence report a thermal conductivity of 179.8 $\mathrm{Wm^{-1}K^{-1}}$ to 219.4 $\mathrm{Wm^{-1}K^{-1}}$. The spread in our prediction is due to using a Lorenz number that ranges from the ideal to a deviation of ∼20% based on reported values of the Lorenz number in previous *ab-initio* simulations [39, 45, 51] and measurements [70]. Ohta *et al.* [23] report a similar value of 226 $\mathrm{Wm^{-1}K^{-1}}$ which has been recently reported to be an overestimate. The corrected value by Lobanov *et al.* [76] is reported as 185 $\mathrm{Wm^{-1}K^{-1}}$ which is in better agreement with our prediction. This is also in the range of recent calculations using a novel non-equilibrium molecular dynamics framework by Yue *et al.* [77] who reported a value of 184 $\mathrm{Wm^{-1}K^{-1}}$ at similar temperature-pressure conditions (P∼137 GPa, T∼3900 K).

Finally in Fig. 3, we consider the electrical DC conductivity as a function of the pressure at various fixed temperatures up to the Earth-core conditions. While not as striking as in Fig. 2, our RT-TDDFT predictions (filled red, orange, light orange, and yellow circles) are closer to the experimental results by Ohta *et al.* (lower filled black and grey squares) and Zhang *et al.* (right filled black squares) then to those by Konôpková *et al.* (upper filled black and grey squares). Note that the Zhang *et al.* data at 4000 K are based on their extrapolation to higher temperatures and pressures using the Bloch-Grüneisen model. Again, we used the Wiedemann-Franz law [73] to extract the DC conductivity from the experimental data by Konôpková *et al.*. We also compare with results obtained from the Bloch-Grüneisen model of Koker *et al.* [39] (red curve), the KG formula by Pozzo *et al.* [45, 46, 63] (red and light orange circles), density functional perturbation theory combined with the Korringa-Kohn-Rostoker method [79, 80] that includes electron-phonon contributions by Xu *et al.* [71] (orange diamond), and dynamical mean field calculations which also capture EES in the BCC and HCP phases of iron by Pourovskii *et al.* [64] (orange squares) and similarly for the HCP phase by He *et al.* [78] (orange triangle). Overall, the change in the conductivity with pressure is predicted to be relatively small by all models and theories.

We conclude this investigation of electronic transport

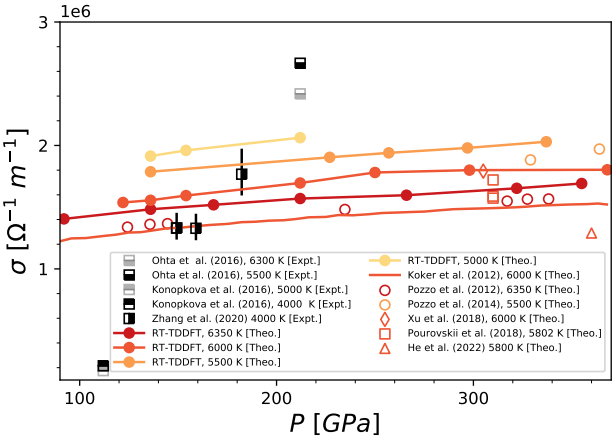

FIG. 3. Electrical conductivity and its pressure dependence at fixed temperature. Results of the experimental diamond anvil cell measurements reported by Ohta *et al.* [23] (lower filled black and grey squares) and Zhang *et al.* [70] (right filled black squares) are contrasted with those by Konôpková *et al.* [24] (upper filled black and grey squares). Our predictions of the electrical conductivity (filled circles) are compared with previously reported calculations, such as the Bloch-Grüneisen model of Koker *et al.* [39] (red curve), the KG formula by Pozzo *et al.* [45, 46] (red and light orange circles), first-principles calculations including electron-phonon contributions by Xu *et al.* [71] (orange diamond), and first-principles calculations including electron-electron and electron-lattice scattering by Pourovskii *et al.* [64] (orange squares) and He *et al.* [78] (orange triangle).

properties by providing a concise assessment of the methods discussed here. We point out that calculations using the KG formula do not include an interaction kernel and, thus, do not take into account collective effects like plasmons. LR-TDDFT is an extension of the KG formula in terms of an interaction kernel. Both the KG formula and LR-TDDFT are often limited to the head of the density response matrix and, therefore, neglect so-called local field effects originating from the off-diagonals. In RT-TDDFT, however, we make no such assumption. Both the complete electronic response and the interaction kernel in terms of Hartree and XC contributions are considered [81].

IV. CONCLUSIONS

In this work, we have reported results on the electrical conductivity of iron under the conditions of Earth's core from the microscopic formulation of Ohm's law. We demonstrate the utility of our method, which is based on the real-time formalism of time-dependent DFT, for computing transport properties in materials under extreme conditions. It provides a viable alternative to current state-of-the-art methods, such as the evaluation of the KG formula on DFT data. We expect our method

to become a widely used device for the interpretation of upcoming free-electron laser scattering experiments at facilities like LCLS [82], the European X-FEL [83], and FLASH [84]. While in this work, the perturbing vector potential was chosen in the linear regime, our method is also valid in the non-linear regime. This will enable studying the response of materials under extreme conditions accessible through recent advances in free-electron lasers [85, 86].

Acknowledgements. — The authors acknowledge Thomas R. Mattsson for his motivation to compare the predictions of TDDFT transport properties with the experimental work on iron under the conditions of Earth's core. This work was partially supported by the Center for Advanced Systems Understanding (CASUS) which is financed by Germanys Federal Ministry of Education and Research (BMBF) and by the Saxon state government out of the State budget approved by the Saxon State Parliament. ML was supported by the German Federal Ministry of Education and Research (BMBF, No. 01/S18026A-F) by funding the competence center for Big Data and AI ScaDS.AI Dresden/Leipzig. Computations were performed on a Bull Cluster at the Center for Information Services and High Performance Computing (ZIH) at Technische Universität Dresden, on the cluster Hemera at Helmholtz-Zentrum Dresden-Rossendorf (HZDR). Sandia National Laboratories is a multimission laboratory managed and operated by National Technology and Engineering Solutions of Sandia, LLC, a wholly-owned subsidiary of Honeywell International Inc., for the U.S. Department of Energys National Nuclear Security Administration under contract DE-NA0003525.

[1] P. A. Frey and G. H. Reed, The ubiquity of iron, ACS Chemical Biology **7**, 1477 (2012), pMID: 22845493, https://doi.org/10.1021/cb300323q.

[2] L. Stixrude, R. E. Cohen, and D. J. Singh, Iron at high pressure: Linearized-augmented-plane-wave computations in the generalized-gradient approximation, Phys. Rev. B **50**, 6442 (1994).

[3] R. Jeanloz, The nature of the earth's core, Annual Review of Earth and Planetary Sciences **18**, 357 (1990).

[4] W. Pepperhoff and M. Acet, *Constitution and Magnetism of Iron and its Alloys* (Springer Science & Business Media, 2013).

[5] G. Morard, D. Andrault, D. Antonangeli, and J. Bouchet, Properties of iron alloys under the earth's core conditions, Comptes Rendus Geoscience **346**, 130 (2014).

[6] H. Hasegawa and D. G. Pettifor, Microscopic theory of the temperature-pressure phase diagram of iron, Phys. Rev. Lett. **50**, 130 (1983).

[7] O. L. Anderson, Properties of iron at the earth's core conditions, Geophysical Journal International **84**, 561 (1986).

[8] L. V. Pourovskii, Electronic correlations in dense iron: from moderate pressure to earths core conditions, Journal of Physics: Condensed Matter **31**, 373001 (2019).

[9] H. Hwang, E. Galtier, H. Cynn, I. Eom, S. Chun, Y. Bang, G. Hwang, J. Choi, T. Kim, M. Kong, *et al.*, Subnanosecond phase transition dynamics in laser-shocked iron, Science Advances **6**, eaaz5132 (2020).

[10] S. White, B. Kettle, J. Vorberger, C. Lewis, S. Glenzer, E. Gamboa, B. Nagler, F. Tavella, H. Lee, C. Murphy, *et al.*, Time-dependent effects in melting and phase change for laser-shocked iron, Physical Review Research **2**, 033366 (2020).

[11] I. A. Kruglov, A. V. Yanilkin, Y. Propad, and A. R. Oganov, Crystal structure prediction at finite temperatures (2021), arXiv:2101.10153 [cond-mat.mtrl-sci].

[12] J. Garai, J. Chen, and G. Telekes, Pvt equation of state of epsilon iron and its densities at inner core conditions, American Mineralogist **96**, 828 (2011).

[13] D. Andrews, Equation of state of the alpha and epsilon phases of iron, Journal of Physics and Chemistry of Solids **34**, 825 (1973).

[14] P. Dorogokupets, A. Dymshits, K. Litasov, and T. Sokolova, Thermodynamics and equations of state of iron to 350 gpa and 6000 k, Scientific reports **7**, 1 (2017).

[15] H. Zhang, S. Lu, M. P. J. Punkkinen, Q.-M. Hu, B. Johansson, and L. Vitos, Static equation of state of bcc iron, Physical Review B **82**, 132409 (2010).

[16] A. Dewaele, P. Loubeyre, F. Occelli, M. Mezouar, P. I. Dorogokupets, and M. Torrent, Quasihydrostatic equation of state of iron above 2 mbar, Physical Review Letters **97**, 215504 (2006).

[17] X. Sha and R. Cohen, First-principles thermal equation of state and thermoelasticity of hcp fe at high pressures, Physical Review B **81**, 094105 (2010).

[18] S. Grant, T. Ao, C. Seagle, A. Porwitzky, J.-P. Davis, K. Cochrane, D. Dolan, J.-F. Lin, T. Ditmire, and A. Bernstein, Equation of state measurements on iron near the melting curve at planetary core conditions by shock and ramp compressions, Journal of Geophysical Research: Solid Earth **126**, e2020JB020008 (2021).

[19] Y. Kuwayama, G. Morard, Y. Nakajima, K. Hirose, A. Q. R. Baron, S. I. Kawaguchi, T. Tsuchiya, D. Ishikawa, N. Hirao, and Y. Ohishi, Equation of state of liquid iron under extreme conditions, Phys. Rev. Lett. **124**, 165701 (2020).

[20] S. Labrosse, Thermal and magnetic evolution of the earths core, Physics of the Earth and Planetary Interiors **140**, 127 (2003).

[21] F. Stacey and D. Loper, A revised estimate of the conductivity of iron alloy at high pressure and implications for the core energy balance, Physics of the Earth and Planetary Interiors **161**, 13 (2007).

[22] H. Gomi, K. Ohta, K. Hirose, S. Labrosse, R. Caracas, M. J. Verstraete, and J. W. Hernlund, The high conductivity of iron and thermal evolution of the earths core, Physics of the Earth and Planetary Interiors **224**, 88 (2013).

[23] K. Ohta, Y. Kuwayama, K. Hirose, K. Shimizu, and Y. Ohishi, Experimental determination of the electrical resistivity of iron at earths core conditions, Nature **534**, 95 (2016).

[24] Z. Konôpková, R. S. McWilliams, N. Gómez-Pérez, and A. F. Goncharov, Direct measurement of thermal conductivity in solid iron at planetary core conditions, Nature **534**, 99 (2016).

[25] R. S. Hixson, M. A. Winkler, and M. L. Hodgdon, Sound speed and thermophysical properties of liquid iron and nickel, Phys. Rev. B **42**, 6485 (1990).

[26] M. Beutl, G. Pottlacher, and H. Jäger, Thermophysical properties of liquid iron, International journal of thermophysics **15**, 1323 (1994).

[27] R. Keeler and A. Mitchell, Electrical conductivity, demagnetization, and the high-pressure phase transition in shock-compressed iron, Solid State Communications **7**, 271 (1969).

[28] G. Gathers, Thermophysical properties of liquid copper and aluminum, International journal of Thermophysics **4**, 209 (1983).

[29] G. Gathers, Dynamic methods for investigating thermophysical properties of matter at very high temperatures and pressures, Reports on Progress in Physics **49**, 341 (1986).

[30] P. Sperling, E. Gamboa, H. Lee, H. Chung, E. Galtier, Y. Omarbakiyeva, H. Reinholz, G. Röpke, U. Zastrau, J. Hastings, *et al.*, Free-electron x-ray laser measurements of collisional-damped plasmons in isochorically heated warm dense matter, Physical review letters **115**, 115001 (2015).

[31] Z. Chen, C. Curry, R. Zhang, F. Treffert, N. Stojanovic, S. Toleikis, R. Pan, M. Gauthier, E. Zapolnova, L. Seipp, *et al.*, Ultrafast multi-cycle terahertz measurements of the electrical conductivity in strongly excited solids, Nature communications **12**, 1 (2021).

[32] D. Dobson, Earth's core problem, Nature **534**, 45 (2016).

[33] M. Berrada and R. A. Secco, Review of electrical resistivity measurements and calculations of fe and fe-alloys relating to planetary cores, Frontiers in Earth Science , 802 (2021).

[34] R. Kubo, Statistical-mechanical theory of irreversible processes. i. general theory and simple applications to magnetic and conduction problems, Journal of the Physical Society of Japan **12**, 570 (1957).

[35] M. P. Desjarlais, J. D. Kress, and L. A. Collins, Electrical conductivity for warm, dense aluminum plasmas and liquids, Phys. Rev. E **66**, 025401 (2002).

[36] K. Plagemann, P. Sperling, R. Thiele, M. Desjarlais, C. Fortmann, T. Döppner, H. Lee, S. H. Glenzer, and R. Redmer, Dynamic structure factor in warm dense beryllium, New Journal of Physics **14**, 055020 (2012).

[37] B. B. L. Witte, L. B. Fletcher, E. Galtier, E. Gamboa, H. J. Lee, U. Zastrau, R. Redmer, S. H. Glenzer, and P. Sperling, Warm dense matter demonstrating non-drude conductivity from observations of nonlinear plasmon damping, Phys. Rev. Lett. **118**, 225001 (2017).

[38] M. Pozzo, M. P. Desjarlais, and D. Alfe, Electrical and thermal conductivity of liquid sodium from first-principles calculations, Physical Review B **84**, 054203 (2011).

[39] N. de Koker, G. Steinle-Neumann, and V. Vlček, Electrical resistivity and thermal conductivity of liquid fe alloys at high p and t, and heat flux in earths core, Proceedings of the National Academy of Sciences **109**, 4070 (2012).

[40] V. c. v. Vlček, N. de Koker, and G. Steinle-Neumann, Electrical and thermal conductivity of al liquid at high pressures and temperatures from ab initio computations, Phys. Rev. B **85**, 184201 (2012).

[41] P. Hohenberg and W. Kohn, Inhomogeneous electron gas, Phys. Rev. **136**, B864 (1964).

[42] W. Kohn and L. J. Sham, Self-consistent equations including exchange and correlation effects, Phys. Rev. **140**, A1133 (1965).

[43] N. D. Mermin, Thermal properties of the inhomogeneous electron gas, Phys. Rev. **137**, A1441 (1965).

[44] J.-A. Korell, M. French, G. Steinle-Neumann, and R. Redmer, Paramagnetic-to-diamagnetic transition in dense liquid iron and its influence on electronic transport properties, Physical review letters **122**, 086601 (2019).

[45] M. Pozzo, C. Davies, D. Gubbins, and D. Alfe, Thermal and electrical conductivity of iron at earths core conditions, Nature **485**, 355 (2012).

[46] M. Pozzo, C. Davies, D. Gubbins, and D. Alfè, Thermal and electrical conductivity of solid iron and iron–silicon mixtures at earth's core conditions, Earth and Planetary Science Letters **393**, 159 (2014).

[47] U. Kleinschmidt, M. French, G. Steinle-Neumann, and R. Redmer, Electrical and thermal conductivity of fcc and hcp iron under conditions of the earth's core from ab initio simulations, Phys. Rev. B **107**, 085145 (2023).

[48] L. Pourovskii, J. Mravlje, A. Georges, S. Simak, and I. Abrikosov, Electron–electron scattering and thermal conductivity of ϵ-iron at earths core conditions, New Journal of Physics **19**, 073022 (2017).

[49] G. Kotliar, S. Y. Savrasov, K. Haule, V. S. Oudovenko, O. Parcollet, and C. A. Marianetti, Electronic structure calculations with dynamical mean-field theory, Rev. Mod. Phys. **78**, 865 (2006).

[50] A. Belozerov and V. Anisimov, Coulomb interaction parameters in bcc iron: an lda+ dmft study, Journal of Physics: Condensed Matter **26**, 375601 (2014).

[51] L. Pourovskii, J. Mravlje, A. Georges, S. Simak, and I. Abrikosov, Electron–electron scattering and thermal conductivity of ε-iron at earths core conditions, New Journal of Physics **19**, 073022 (2017).

[52] E. K. U. Gross and W. Kohn, Local density-functional theory of frequency-dependent linear response, Phys. Rev. Lett. **55**, 2850 (1985).

[53] K. Ramakrishna, A. Cangi, T. Dornheim, A. Baczewski, and J. Vorberger, First-principles modeling of plasmons in aluminum under ambient and extreme conditions, Phys. Rev. B **103**, 125118 (2021).

[54] T. Dornheim, A. Cangi, K. Ramakrishna, M. Böhme, S. Tanaka, and J. Vorberger, Effective static approximation: A fast and reliable tool for warm-dense matter theory, Phys. Rev. Lett. **125**, 235001 (2020).

[55] M. Marques and E. Gross, Time-dependent density functional theory, Annual Review of Physical Chemistry **55**, 427 (2004).

[56] K. Yabana and G. F. Bertsch, Time-dependent local-density approximation in real time, Phys. Rev. B **54**, 4484 (1996).

[57] A. Castro, H. Appel, M. Oliveira, C. A. Rozzi, X. Andrade, F. Lorenzen, M. A. Marques, E. Gross, and A. Rubio, Octopus: a tool for the application of time-dependent density functional theory, physica status solidi (b) **243**, 2465 (2006).

[58] C. A. Ullrich, *Time-dependent density-functional the-*

ory: concepts and applications (OUP Oxford, 2011).
[59] G. F. Bertsch, J.-I. Iwata, A. Rubio, and K. Yabana, Real-space, real-time method for the dielectric function, Physical Review B **62**, 7998 (2000).
[60] A. D. Baczewski, L. Shulenburger, M. Desjarlais, S. Hansen, and R. Magyar, X-ray thomson scattering in warm dense matter without the chihara decomposition, Physical review letters **116**, 115004 (2016).
[61] X. Andrade, S. Hamel, and A. A. Correa, Negative differential conductivity in liquid aluminum from real-time quantum simulations, The European Physical Journal B **91**, 229 (2018).
[62] K. Ramakrishna, M. Lokamani, A. Baczewski, J. Vorberger, and A. Cangi, Electrical and thermal conductivity of high-pressure solid iron (2022), arXiv:2210.10132 [cond-mat.mtrl-sci].
[63] M. Pozzo, C. Davies, D. Gubbins, and D. Alfè, Transport properties for liquid silicon-oxygen-iron mixtures at earth's core conditions, Phys. Rev. B **87**, 014110 (2013).
[64] L. Pourovskii, J. Mravlje, M. Pozzo, and D. Alfè, Electronic correlations and transport in iron at earths core conditions, Nature communications **11**, 1 (2020).
[65] D. J. Singh and L. Nordstrom, *Planewaves, Pseudopotentials, and the LAPW method* (Springer Science & Business Media, 2006).
[66] J. K. D. et al., Elk, all-electron full-potential linearised augmented plane wave (fp-lapw) code, `http://elk.sourceforge.net` (2022).
[67] A. Gulans, S. Kontur, C. Meisenbichler, D. Nabok, P. Pavone, S. Rigamonti, S. Sagmeister, U. Werner, and C. Draxl, Exciting: a full-potential all-electron package implementing density-functional theory and many-body perturbation theory, Journal of Physics: Condensed Matter **26**, 363202 (2014).
[68] R. R. Pela and C. Draxl, All-electron full-potential implementation of real-time tddft in exciting, Electronic Structure (2021).
[69] See Supplemental Material for additional information which includes Refs. [43, 81, 87–100].
[70] Y. Zhang, M. Hou, G. Liu, C. Zhang, V. B. Prakapenka, E. Greenberg, Y. Fei, R. E. Cohen, and J.-F. Lin, Reconciliation of experiments and theory on transport properties of iron and the geodynamo, Phys. Rev. Lett. **125**, 078501 (2020).
[71] J. Xu, P. Zhang, K. Haule, J. Minar, S. Wimmer, H. Ebert, and R. E. Cohen, Thermal conductivity and electrical resistivity of solid iron at earth's core conditions from first principles, Phys. Rev. Lett. **121**, 096601 (2018).
[72] F. D. Stacey and O. L. Anderson, Electrical and thermal conductivities of fe–ni–si alloy under core conditions, Physics of the Earth and Planetary Interiors **124**, 153 (2001).
[73] R. Franz and G. Wiedemann, Ueber die wrmeleitungsfhigkeit der metalle, Annalen der Physik **165**, 497 (1853).
[74] D. Jaccard, A. Holmes, G. Behr, Y. Inada, and Y. Onuki, Superconductivity of ε-fe: complete resistive transition, Physics Letters A **299**, 282 (2002).
[75] C. T. Seagle, E. Cottrell, Y. Fei, D. R. Hummer, and V. B. Prakapenka, Electrical and thermal transport properties of iron and iron-silicon alloy at high pressure, Geophysical Research Letters **40**, 5377 (2013).
[76] S. S. Lobanov and Z. M. Geballe, Non-isotropic contraction and expansion of samples in diamond anvil cells: Implications for thermal conductivity at the core-mantle boundary, Geophysical Research Letters **49**, e2022GL100379 (2022).
[77] S.-Y. Yue and M. Hu, Insight of the thermal conductivity of ϵ-iron at earths core conditions from the newly developed direct ab initio methodology, Journal of Applied Physics **125**, 045102 (2019).
[78] Y. He, S. Sun, D. Y. Kim, B. G. Jang, H. Li, and H.-k. Mao, Superionic iron alloys and their seismic velocities in earths inner core, Nature **602**, 258 (2022).
[79] J. Korringa, On the calculation of the energy of a bloch wave in a metal, Physica **13**, 392 (1947).
[80] W. Kohn and N. Rostoker, Solution of the schrödinger equation in periodic lattices with an application to metallic lithium, Physical Review **94**, 1111 (1954).
[81] A. D. Baczewski, T. Hentschel, A. Kononov, and S. B. Hansen, Predictions of bound-bound transition signatures in x-ray thomson scattering (2021), arXiv:2109.09576 [physics.plasm-ph].
[82] L. B. Fletcher, H. J. Lee, T. Döppner, E. Galtier, B. Nagler, P. Heimann, C. Fortmann, S. LePape, T. Ma, M. Millot, A. Pak, D. Turnbull, D. A. Chapman, D. O. Gericke, J. Vorberger, T. White, G. Gregori, M. Wei, B. Barbrel, R. W. Falcone, C.-C. Kao, H. Nuhn, J. Welch, U. Zastrau, P. Neumayer, J. B. Hastings, and S. H. Glenzer, Ultrabright x-ray laser scattering for dynamic warm dense matter physics, Nature Photonics **9**, 274 (2015).
[83] T. Tschentscher, C. Bressler, J. Grnert, A. Madsen, A. P. Mancuso, M. Meyer, A. Scherz, H. Sinn, and U. Zastrau, Photon beam transport and scientific instruments at the european xfel, Applied Sciences **7**, 10.3390/app7060592 (2017).
[84] U. Zastrau, P. Sperling, M. Harmand, A. Becker, T. Bornath, R. Bredow, S. Dziarzhytski, T. Fennel, L. Fletcher, E. Förster, S. Göde, G. Gregori, V. Hilbert, D. Hochhaus, B. Holst, T. Laarmann, H. Lee, T. Ma, J. Mithen, R. Mitzner, C. Murphy, M. Nakatsutsumi, P. Neumayer, A. Przystawik, S. Roling, M. Schulz, B. Siemer, S. Skruszewicz, J. Tiggesbäumker, S. Toleikis, T. Tschentscher, T. White, M. Wöstmann, H. Zacharias, T. Döppner, S. Glenzer, and R. Redmer, Resolving Ultrafast Heating of Dense Cryogenic Hydrogen, Phys. Rev. Lett. **112**, 105002 (2014).
[85] U. Zastrau, K. Appel, C. Baehtz, O. Baehr, L. Batchelor, A. Berghäuser, M. Banjafar, E. Brambrink, V. Cerantola, T. E. Cowan, *et al.*, The high energy density scientific instrument at the european xfel, Journal of synchrotron radiation **28** (2021).
[86] V. Cerantola, A. D. Rosa, Z. Konôpková, R. Torchio, E. Brambrink, A. Rack, U. Zastrau, and S. Pascarelli, New frontiers in extreme conditions science at synchrotrons and free electron lasers, Journal of Physics: Condensed Matter **33**, 274003 (2021).
[87] G. Kresse and J. Hafner, Ab initio molecular dynamics for liquid metals, Phys. Rev. B **47**, 558 (1993).
[88] G. Kresse and D. Joubert, From ultrasoft pseudopotentials to the projector augmented-wave method, Phys. Rev. B **59**, 1758 (1999).
[89] G. Kresse and J. Furthmüller, Efficiency of ab-initio total energy calculations for metals and semiconductors using a plane-wave basis set, Computational Materials Science **6**, 15 (1996).

[90] G. Kresse and J. Furthmüller, Efficient iterative schemes for ab initio total-energy calculations using a plane-wave basis set, Phys. Rev. B **54**, 11169 (1996).
[91] P. E. Blöchl, Projector augmented-wave method, Physical review B **50**, 17953 (1994).
[92] J. P. Perdew, K. Burke, and M. Ernzerhof, Generalized gradient approximation made simple, Physical review letters **77**, 3865 (1996).
[93] W. G. Hoover, Canonical dynamics: Equilibrium phase-space distributions, Phys. Rev. A **31**, 1695 (1985).
[94] R. G. Kraus, R. J. Hemley, S. J. Ali, J. L. Belof, L. X. Benedict, J. Bernier, D. Braun, R. E. Cohen, G. W. Collins, F. Coppari, M. P. Desjarlais, D. Fratanduono, S. Hamel, A. Krygier, A. Lazicki, J. Mcnaney, M. Millot, P. C. Myint, M. G. Newman, J. R. Rygg, D. M. Sterbentz, S. T. Stewart, L. Stixrude, D. C. Swift, C. Wehrenberg, and J. H. Eggert, Measuring the melting curve of iron at super-earth core conditions, Science **375**, 202 (2022).
[95] G. Morard, S. Boccato, A. D. Rosa, S. Anzellini, F. Miozzi, L. Henry, G. Garbarino, M. Mezouar, M. Harmand, F. Guyot, *et al.*, Solving controversies on the iron phase diagram under high pressure, Geophysical Research Letters **45**, 11 (2018).
[96] S. Anzellini, A. Dewaele, M. Mezouar, P. Loubeyre, and G. Morard, Melting of iron at earths inner core boundary based on fast x-ray diffraction, Science **340**, 464 (2013).
[97] L. Stixrude, Structure of iron to 1 gbar and 40 000 k, Physical Review Letters **108**, 055505 (2012).
[98] S. Tateno, K. Hirose, Y. Ohishi, and Y. Tatsumi, The structure of iron in earths inner core, Science **330**, 359 (2010).
[99] Y. Ma, M. Somayazulu, G. Shen, H.-k. Mao, J. Shu, and R. J. Hemley, In situ x-ray diffraction studies of iron to earth-core conditions, Physics of the Earth and Planetary Interiors **143**, 455 (2004).
[100] R. A. Paquin, Properties of metals, Handbook of optics **2**, 35 (1995).